AGU PUBLICATIONS

Water Resources Research

RESEARCH ARTICLE

10.1002/2013WR014283

Extrapolating active layer thickness measurements across Arctic polygonal terrain using LiDAR and *NDVI* data sets

Chandana Gangodagamage[1], Joel C. Rowland[1], Susan S. Hubbard[2], Steven P. Brumby[1], Anna K. Liljedahl[3], Haruko Wainwright[2], Cathy J. Wilson[1], Garrett L. Altmann[1], Baptiste Dafflon[2], John Peterson[2], Craig Ulrich[2], Craig E. Tweedie[4], and Stan D. Wullschleger[5]

[1]Los Alamos National Laboratory, Los Alamos, New Mexico, USA, [2]Lawrence Berkeley National Laboratory, Berkeley, California, USA, [3]Water and Environmental Research Center and International Arctic Research Center, University of Alaska Fairbanks, Fairbanks, Alaska, USA, [4]Department of Biological Sciences, University of Texas at El Paso, El Paso, Texas, USA, [5]Oak Ridge National Laboratory, Oak Ridge, Tennessee, USA

Key Points:
- First effort to map the ALT using fine resolution remotely sensed data
- A blended methodology incorporating RS data and statistical manipulation
- Smaller-scale ALT is controlled by eco-hydro-geo variables

Correspondence to:
C. Gangodagamage,
chhandana@gmail.com

Citation:
Gangodagamage, C., et al. (2014), Extrapolating active layer thickness measurements across Arctic polygonal terrain using LiDAR and *NDVI* data sets, *Water Resour. Res.*, *50*, 6339–6357, doi:10.1002/2013WR014283.

Received 24 JUN 2013
Accepted 2 JUL 2014
Accepted article online 8 JUL 2014
Published online 5 AUG 2014

Abstract Landscape attributes that vary with microtopography, such as active layer thickness (*ALT*), are labor intensive and difficult to document effectively through in situ methods at kilometer spatial extents, thus rendering remotely sensed methods desirable. Spatially explicit estimates of *ALT* can provide critically needed data for parameterization, initialization, and evaluation of Arctic terrestrial models. In this work, we demonstrate a new approach using high-resolution remotely sensed data for estimating centimeter-scale *ALT* in a 5 km^2 area of ice-wedge polygon terrain in Barrow, Alaska. We use a simple regression-based, machine learning data-fusion algorithm that uses topographic and spectral metrics derived from multisensor data (LiDAR and WorldView-2) to estimate *ALT* (2 m spatial resolution) across the study area. Comparison of the *ALT* estimates with ground-based measurements, indicates the accuracy ($r^2 = 0.76$, RMSE ± 4.4 cm) of the approach. While it is generally accepted that broad climatic variability associated with increasing air temperature will govern the regional averages of *ALT*, consistent with prior studies, our findings using high-resolution LiDAR and WorldView-2 data, show that smaller-scale variability in *ALT* is controlled by local eco-hydro-geomorphic factors. This work demonstrates a path forward for mapping *ALT* at high spatial resolution and across sufficiently large regions for improved understanding and predictions of coupled dynamics among permafrost, hydrology, and land-surface processes from readily available remote sensing data.

1. Introduction

Most general circulation models predict that warming observed in the Arctic over the past decades [*Hassol et al.*, 2004] will continue and is likely to accelerate through the 21st century [*IPCC*, 2013]. This warming will be accompanied by a thawing of permafrost and an increase in the thickness of the active layer [*Koven et al.*, 2013; *Slater and Lawrence*, 2013; *Streletskiy et al.*, 2012; *Lawrence et al.*, 2008], which is the layer of soil that experiences seasonal freeze and thaw. Increased active layer thickness (*ALT*) will be accompanied by changes in hydrology (inundation patterns and soil moisture) [*Hinzman et al.*, 2005], vegetation [*Chapin et al.*, 1988], surface energy balance [*Porter et al.*, 2011], and geomorphology (thermal erosion, landslides, ground subsidence, and possibly channel development) [*Gooseff et al.*, 2009; *Rowland et al.*, 2010; *Gangodagamage et al.*, 2007]. Most geomorphic, hydrological, soil microbial, and biogeochemical activities are limited to the active layer [*Brown et al.*, 1980; *Hinzman and Kane*, 1991], which may vary from 30 to substantially higher than 70 cm, depending on geographic location [*Hinkel and Nelson*, 2003; *Zhang et al.*, 2005; *Shiklomanov et al.*, 2010]. The potential release of carbon into the atmosphere as the active layer thickens is of great concern; it is estimated that 1672 Pg of carbon are currently stored in permafrost, with the vast majority in the upper 3 m [*Tarnocai et al.*, 2009]. However, in current climate-model predictions of *ALT* response to future warming, the permafrost landscape is represented at a relatively coarse resolution, and microtopographic variations are often ignored [*Lu and Zhuang*, 2012]. Methods of quantifying *ALT*s at fine spatial resolution across large spatial scales, therefore, have the potential to refine assessments of the rate and timing of pan-Arctic soil carbon releases.

ALT depends on many climatological parameters, such as air temperature, surface temperature, and snow thickness [*Smith*, 1975], as well as on land-surface properties such as surface morphology (slope, aspect)

[*Nelson et al*., 1997], vegetation cover, and the physical, hydrological, and thermal properties of the surface cover and subsurface [*Brown et al*., 2000; *Zhang et al*., 2005]. *ALT* is usually directly measured by inserting a metal probe through the seasonally thawed soil to resistance at the top of permafrost, or by collecting ground temperatures from vertical arrays of temperature sensors [*Brown et al*., 2000]. Thaw tubes are another common method used in Canada to measure *ALT* [*Mackay*, 1973]; they primarily measure maximum annual thaw penetration and maximum annual heave and ground subsidence [*Rickard and Brown*, 1972; *Mackay*, 1973; *Nixon et al*., 1995]. Thaw tubes track the maximum annual thaw depth as the maximum depth penetration of a colored marker along a tube of water inserted into the ground. During the thaw season, the marker sinks through water to the depth at the top of the permafrost table where the water in tube remains frozen [*Nixon et al*., 1995].

Thaw depths may also be estimated using analytical procedures such as a specific form of the Stefan solution [*Harlan and Nixon*, 1978]. Using this method the seasonal thaw depths (X) are linked to the accumulated surface thawing-degree days ($ATDD_s$), which is the daily average of the surface temperatures from the beginning of thaw onset to the date of active layer measurement:

$$X = \sqrt{\left(2k\frac{ATDD_s}{L}\right)} \tag{1}$$

where X is thaw depth (m), k is the unfrozen thermal conductivity of soil ($Wm^{-1}\ K^{-1}$), $ATDD_s$ is surface thawing-degree day (°C), and L is the volumetric latent heat of fusion (Jm^{-3}). Here, thaw depth is a function of the accumulated seasonal thawing temperature, along with substrate moisture content and thermal properties. $ATDD_s$ at a site is usually derived from accumulated air thawing-degree day ($ATDD$) and the thawing "*n* factor" (n_T), which are usually related to $ATDD_s$ by an empirical equation given as $ATDD_s = n_T{*}ATDD$ [*Lanardini*, 1978]. This analytical technique is extensively used to cross validate the *ALTs* measured from probing or thaw tubes [*Shiklomanov et al*., 2010; *Smith et al*., 2009]. Here, n_T is determined using field data [*Taylor*, 2000]. A strong correlation between measured landscape-specific *ALT* and $\sqrt{(ATDD_s)}$ was observed for the CALM (Circumpolar Active Layer Monitoring network) site at Barrow, Alaska [*Shiklomanov et al*., 2010].

While these methods used to measure *ALT* are accurate, they are labor intensive and limited in spatial coverage. At regional scales, attempts have been made to model *ALT* by extrapolating ground measurements using empirical and statistical relationships with air temperature, ground temperature, elevation, and surface vegetation at coarser (30–300 m) spatial resolution [*Nelson et al*., 1997, 1999; *Zhang et al*., 1997; *Shiklomanov and Nelson*, 1999]. Working at the same site as this study, *Hubbard et al*. [2013] showed that surface ground-penetrating-radar data could be used to provide very high resolution and accurate estimates of *ALT*. They also found that *ALT*, as well as other geochemical, geophysical, hydrogeological and thermal properties, varied spatially as a function of polygon type, or "geomorphic zonation." Most recently, *Liu et al*. [2012] estimated *ALTs* across an 80 by 100 km^2 area of the North Slope of Alaska, at a 100 m resolution using InSAR. They related InSAR-derived surface subsidence-to-volumetric changes associated with freeze and thaw of a saturated soil column. This method assumed the active layer was close to fully saturated, and it required some knowledge of soil and land-cover characteristics for estimating water content of the soils.

While current methods are very good at quantifying and predicting *ALT* at either local or regional scales, no method has been presented that is able to capture both the fine scale variation in *ALT* related to the microtopography of rims, troughs, and centers in ice wedge polygon landscapes, and the influence of microtopography on *ALT* over large spatial domains. Since *ALT* can vary by tens of centimeters over small spatial scales, improved representation of *ALT* variation has the potential to improve regional scale predictions of hydrologic response and carbon fluxes in ice wedge polygon landscapes [*Minke et al*., 2009; *Zona et al*., 2011; *Hubbard et al*., 2013].

Here, we present a new approach for estimating *ALT* at high spatial resolution (2 m), using remotely sensed data sets and ground-truth data (*ALT* by probing). We employed a multisensor data-fusion approach, using statistical learning from a simple, multivariate, piecewise regression technique [*Berk*, 2008], by combining in situ *ALT* measurements with (a) data sets from LiDAR-derived high-resolution surface elevation (0.25 m) to obtain local slope and landscape curvature, and (b) high resolution (2 m) Worldview-2 (DigitalGlobe, Inc.) data to obtain the Normalized Difference Vegetation Index (*NDVI*). We used a statistical machine-learning

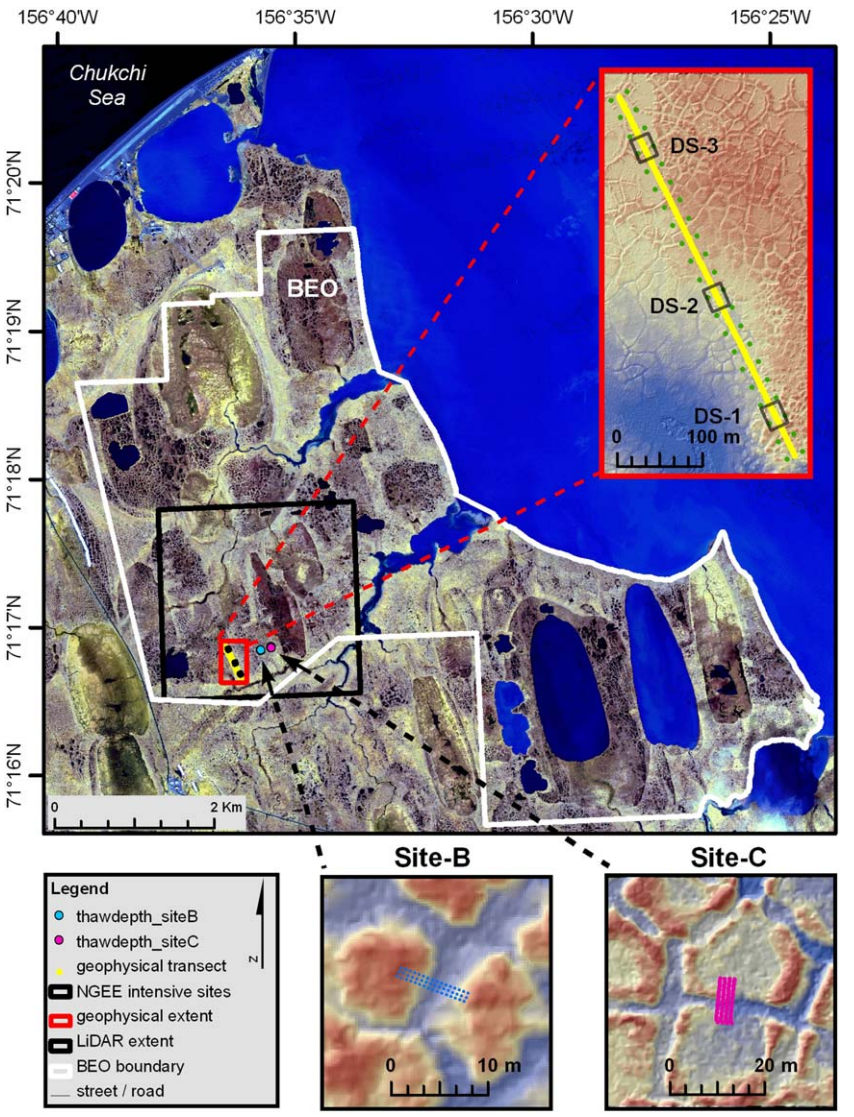

Figure 1. Study area enclosed within the Barrow Environmental Observatory (BEO) (white), the LiDAR data extent (black), the geophysical transect described by *Hubbard et al*. [2013] (yellow), and the locations of NGEE extensive field experimental site B (blue) and C (red).

method to relate the surface data to the direct *ALT* measurements. The proposed method offers the potential to provide *ALT* estimates at high spatial resolution and across sufficiently large regions for improved understanding and predictions of coupled dynamics among permafrost, hydrology, and land-surface processes.

2. Study Area and Data Collection

The study site is located within the Barrow Environmental Observatory, BEO, near the city of Barrow, Alaska (71.3°N, 156.5°W), which is approximately 6 km southwest of the northernmost point of Alaska and is on the Alaskan arctic coastal plain (Figure 1). In this paper, we will refer to the study site as "Barrow" even though the BEO is located to the southeast of the city of Barrow, AK. At Barrow, the mean annual adjusted precipitation is about 173 mm yr^{-1}, and mean annual air temperature is −12°C, [*Liljedahl et al*., 2011], with a minimum mean monthly temperature of −26.6°C in February and maximum mean monthly temperature of 4.7°C in July [*NCDC*, 2002]. Permafrost underlies the entire area and extends to depths of 300 m or greater [*Brewer*, 1958], with *ALT* varying from 20 to 70 cm [*Shiklomanov et al*., 2010]. The depth at which the zero annual amplitude of soil temperature (permafrost temperature) in Barrow is approximately 15 m

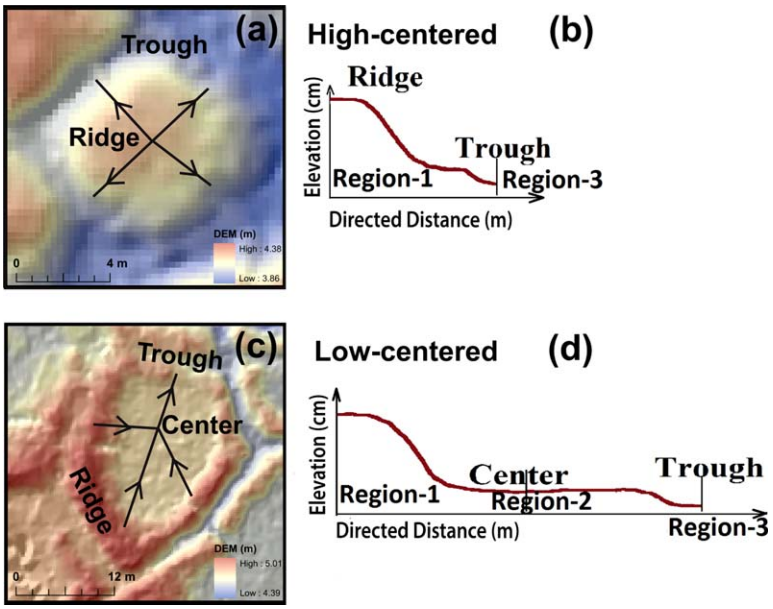

Figure 2. A schematic of how directed distance (DD) is used as a scale parameter for a high centered and a low centered polygon. DD in (a) high centered (HC) polygon and (b) the corresponding general elevation profile for a high centered (HC) polygon. DD in (c) a low centered (LC) polygon and (d) the corresponding general elevation profile for a low centered (LC) polygon.

[*Romanovsky et al*., 2002]. Permafrost temperature has increased by 1°C in Barrow from 1950 to 2001. However, no associated trend in *ALT* has been observed in Barrow, Alaska [*Romanovsky et al*., 2002] until 2005. The most recent active layer data collected at two CALM sites at Barrow, Alaska (see the data for site code U1 at http://www.gwu.edu/∼calm/data/webforms/u1_f.htm and site code U2 at http://www.gwu.edu/∼calm/data/webforms/u2_f.htm) show progressive increase in *ALT* since 2005.

Vegetation patterns at Barrow vary with ice-wedge polygon topography and surface hydrology [*Britton*, 1957; *Bliss and Peterson*, 1992]. A variety of ice-wedge polygon morphologies exists in the area [*Brown et al*., 1980]. Here we focused on a 5 km^2 area encompassing low centered (LC) and high centered (HC) polygons (Figures 2 and 3); this is the same region described by *Hubbard et al*. [2013]. Within our study area, there is a dramatic contrast in vegetation type across polygon rims, troughs, and centers. Mosses, lichen, and dwarf

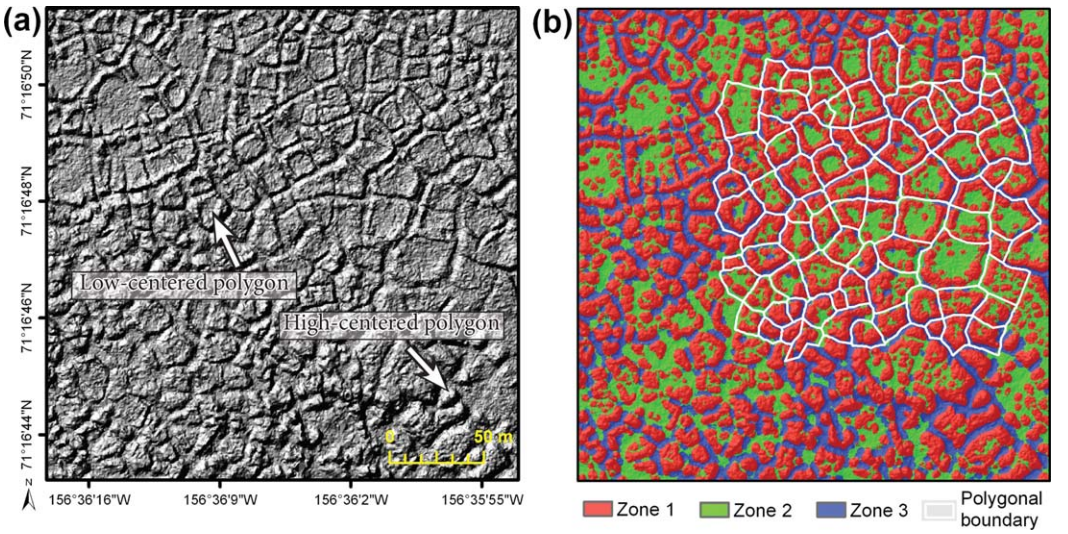

Figure 3. (a) A shaded relief map of high centered (HC) and low centered (LC) polygons. Arrow lines indicate an example for a typical high centered polygon and a low centered polygon. (b) A map of Zone 1, Zone 2, and Zone 3 are shown. White color polygons show the delineated polygon boundaries from the LiDAR data.

shrubs mainly cover elevated areas of HC polygon centers and LC polygon rims, while mosses and sedges with standing water are found in depressions of troughs and LC polygon centers [*Webber*, 1978; *Villarreal et al*., 2012]. These land-cover types can alter the surface energy balance and thermal properties in microtopographic regions, through changes in albedo, surface roughness, and evapotranspiration [*Langer et al*., 2010; *Villarreal et al*., 2012]. Low landscape relief (<7 m; Figure 2) and low hydraulic gradient characterize this landscape.

The soil properties of the coastal tundra at Barrow site are products of both climate factors and the specific geological history of the area. Data gathered from nine sites during the international tundra biomes effort have shown that the soil at Barrow is similar to other tundra areas [*French*, 1974]. Barrow soil types are generally classified as Gelisols, which primarily includes an organic-rich soil layer underlined by a cryoturbated mineral soil (silty clay to silty loam-textured) layer, and a frozen organic-rich mineral layer [*Bockheim et al*., 1999; *Drew*, 1957].

Soil formation at Barrow is associated with the seasonal freeze and thaw processes in ice-wedge polygons at low annual temperatures, high relative moisture conditions, and low mean annual precipitations under impeded drainage conditions [*Gersper et al*., 1980]. Based on climate and soil factors, *Rosswall and Heal* [1975] documented that coastal tundra soil types are highly correlated with the microtopographic units. Their classification indicated the occurrence of uniform soil classes within meadows, polygon troughs, rims, center areas of low centered polygons, and centers of high centered polygons. The texture of the mineral soil is relatively uniform across all microtopographic zonations [*Hubbard et al*., 2013].

A unique characteristic of the tundra soils is the high amount of organic matter, which influences the fluxes of soil, heat, gases (like oxygen, CO_2, and methane), and cation exchange [*Babb and Whitfield*, 1977; *Chapin and Van Cleve*, 1978]. One-third of this organic matter is in the upper 10 cm of soil [*Gersper et al*., 1980]. Variability in soil organic carbon (SOC) has also been documented in soils across ice-wedge polygon landscapes at Barrow. SOC varied from 24 to 28 kg m^{-3} in troughs (both in HC and LC polygons) whereas these values in polygon rims and centers have been documented at 32 and 84 kg m^{-3}, respectively [*Bockheim et al*., 1999].

For this study, in situ thaw depth data were collected at three areas using the mechanical probing method (inserting a metal probe through the active layer to resistance at the top of the permafrost) in conjunction with a detailed laser level and differential GPS survey as part of the Department of Energy Next-Generation Ecosystem Experiments Arctic (DOE NGEE-Arctic) project. The survey area was (1) a 475 m long transect with one thaw-depth measurement every 3 m, three detailed short transects measurements at 0.5 m interval along the same transect (Figure 1), and two 475 m long 10 m offset transect measurements every 25 m (a total of 300 points, uniform sampling; 24 September to 1 October 2011); and (2) two areas (Site B and Site C) with multiple shorter transects (<10 m) each having one measurement every 0.5 m (108 points; Figure 1). The direction (NW-SE) of the 475 m transect was intended to capture a variety of polygon types, with the southern portion encompassing HC polygons and the northern portion LC polygons. A more spatially intensive sampling effort along the 475 m transect was performed at sites DS1, DS2, and DS3 (Figure 1; 0.5 m intervals, i.e., a total of 99 point measurements). The thaw-depth measurements were considered equivalent to *ALT* due to the timing of early fall field campaigns.

High-resolution LiDAR data (0.25 m spatial resolution) were collected on 4 October 2005. The LiDAR data's horizontal and vertical accuracy were approximately 0.30 and 0.15 m, respectively. This LiDAR data were quality-checked in late August 2006 by Siebert and Associates (http://seibert-ak.com/gps); 284 data points were used for this purpose. This survey indicated a systematic error of −0.143 m, which was then used to correct the LiDAR point cloud data.

3. Methodology

3.1. Creating a Spatial Database for Modeling

Four explanatory variables derived from remotely sensed data were used to predict *ALT*: (1) directed distance (*DD*, m), (2) local slope (*S*, m/m), (3) curvature derived from wavelet transformation (wavelet curvature; *WC*, 1/m), and (4) *NDVI*. The *DD*, *S*, and *WC* were used to parameterize the geomorphic variability associated with *ALT*. *NDVI* was used to characterize the vegetation cover, standing dead vegetation, and soil moisture regimes of the polygonal landscape.

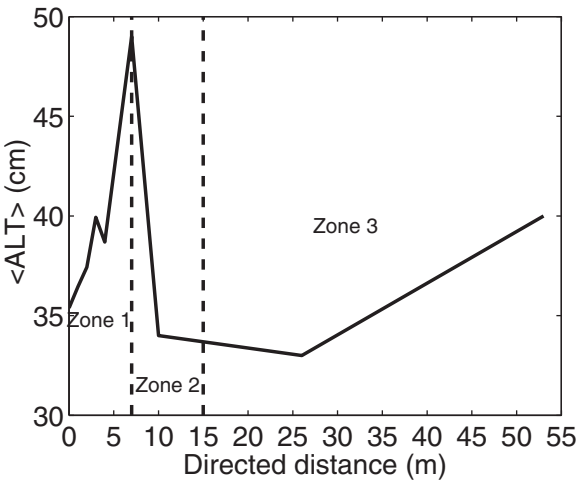

Figure 4. The relationship between ensemble averaged *ALT* (<*ALT*>) and directed distance measured along the flow paths for both low centered and high centered polygons. ALT values were averaged as a function of directed distance measured along the high centered and low centered flow paths.

Gangodagamage et al. [2011] first introduced *DD* in the analysis of river basins, where they related the ensemble average-basin attributes (e.g., slope, curvature) to the distance of any given pixel from the nearest drainage divide. In areas of HC polygons, *DD* was calculated from the elevated polygon center to the trough along the downstream surface flow paths (Figures 2a and 2b). The *DD* associated with LC polygons was calculated starting at the elevated rims along the downward surface flow path, i.e., from the polygon rims to the surrounding trough directly or through the polygon centers (Figures 2c and 2d). We used *DD* to define the topographic position of the *ALT* field measurements. Further, *DD* is used to separate topographic attributes into categories defined by values of slope, wavelet curvature, and *NDVI*, which are then analyzed for trends and relationships that each variable makes with measured values of *ALT*.

For all *ALT* measurements, we computed the *DD* along the microtopographic flow paths. We then computed the ensemble mean *ALT* (<*ALT*>) as a function of *DD* (Figure 2). Linear relationships between *ALT* field measurements and the morphological characteristics of the polygons defined three microtopographic zones (Figure 4). In LC polygons, Zone 1 ($0 \leq DD \leq 7$) encompassed the polygon rim, slope inflection point, and lower slope of the rim within the interior of the polygons (Figure 3b red area). For HC polygons, Zone 1 included the polygon center (flow characteristics are similar to polygon rim points of LC polygons), slope inflection points, and lower slope areas at the polygon-trough boundary (Figures 3a and 3b). Zone 2 ($7 < DD \leq 15$) in LC polygons included the low interior portion of the polygon and typically extended to the lowest points at the polygon boundary along the downstream *DD* flow paths (Figures 3a and 3b). HC polygon morphology was typically different from LC polygons, and Zone 2 was not represented in HC polygons. For all polygon types, Zone 3 ($DD > 15$) represented the troughs.

The local slope was computed by considering a region composed of nine (0.75×0.75 m^2) grid cells, whereas the curvature was computed by convolving a second derivative of the Gaussian wavelet (also called Mexican Hat Wavelet) with the elevation data set [*Lashermes et al*., 2007]. Imagery used for the calculation of *NDVI* was from the WorldView-2 (DigitalGlobe, Inc.) satellite with eight multispectral bands (coastal, Band 1, 400–450 nm; blue, Band 2, 450–510 nm; green, Band 3, 510–580 nm; yellow, Band 4, 585–625 nm; red, Band 5, 630–690 nm; red edge, Band 6, 705–745 nm; near infrared 1 (NIR 1), Band 7, 770–895 nm; near infrared 2 (NIR 2), Band 8, 860–1040 nm). We used ENVI version 4.8 (Exelis Visual Information Solutions, Boulder, Colorado) to orthorectify the WorldView-2 images using RPC (rational polynomial coefficients), LiDAR elevation data, and ground control points (GPC are collected by a GPS survey conducted by Aerometrics Inc.) to authorectify the WorldView-2 data. The pixel digital numbers (DN) of the data were converted to spectral radiances for better quantitative representation of spectral responses. The DN values were initially converted to top-of-atmosphere spectral radiance ($Wm^{-2}\ sr^{-1}\ \mu m^{-1}$), using absolute radiometric calibration factors ($Wm^{-2}\ sr^{-1}\ count^{-1}$) given for each band to get a band integrated radiance ($Wm^{-2}\ sr^{-1}$), which were then normalized by effective bandwidth to get the spectral radiance [*Updike and Comp*, 2010]. We used the red band (Band 5, 630–690 nm) and near-infrared band (Band 7, 770–895 nm) to compute the *NDVI* (spatial resolution 2 m) values from an image acquired on 21 July 2010.

Thaw depths during early fall were collected using a T-handled tile probe labeled in centimeter gradations from the bottom of the probe to the top. The probe used was 1.5 m long and 1 cm in diameter with a

tapered tip. The probe was strong enough to resist the bending stress generated by the resistance of the substrate material in the active layer (for $ALT < 1$ m). No rocks or other hard materials were found in the substrate, and the substrate soils were so wet as it is rich in ice content in this Barrow site. The probe was pushed into the soil until the downward movement ceased when the tip reached the permafrost table. Then, the tip of the probe was raised a few centimeters and pushed downward to confirm the position of the permafrost table. The depth was recorded at this position to the nearest centimeter. A TOPCON GRS-1 (Geodetic Rover System) real-time kinematic global positioning system (RTK GPS) was used to measure the latitude, longitude, and elevation at all *ALT* measurements locations. All positional data collection showed subcentimeter accuracy in both vertical and horizontal directions [*Hubbard et al*., 2013].

3.2. Relative Accuracy of LiDAR and LiDAR-Derived Products

The increasing availability of high-resolution (1 m) topography data and enhanced computational processing power presents new opportunities to study landscape processes quantitatively, in detail not possible before. Given this new power, it is now of utmost importance to understand how these LiDAR and LiDAR-derived metrics (such as slope, curvature), as well as high-resolution satellite-data-derived products (such as normalized difference vegetation index—*NDVI*) influence high-resolution model predictions. In the following section, we review the absolute and relative accuracies of the LiDAR data and investigate how it influences the accuracies in LiDAR-derived products such as *DD*, *NDD*, slope, and curvature.

3.2.1. Absolute Accuracy

Accuracy of a DEM (Digital Elevation Model) derived from LiDAR depends on many factors: LiDAR sensor (pulse length and rate, wavelength, and scan angle), aircraft (altitude and speed), navigation system (GPS system), LiDAR point processing and labeling, and geographic location (seasonality, land-cover, and terrain slope) [*ASPRS*, 2004; *Hodgson et al*., 2005; *Shrestha et al*., 1999]. Vertical accuracy is the principal criterion in determining the quality of the elevation data, with the accuracy requirement primarily depending upon the respective user applications [*Hodgson and Bresnahan*, 2004]. At the preliminary data-calibration stage, errors associated with yaw, pitch, and role of the aircraft are assessed and corrected by the LiDAR data provider. The vertical absolute accuracy of a data set is then derived by computing the root-mean-square error ($RMSE_z$) of the elevation data:

$$RMSE_z = \sqrt{\left(\frac{1}{n}\sum_{i=1}^{n}\left(Z(i)_{LiDAR} - Z(i)_{DGPS}\right)^2\right)} \quad (2)$$

Here, n is the number of points used for the accuracy assessment and $RMSE_Z$ is a summation of LiDAR system error, error in DPGS survey, error associated with different topographic slopes, and error due to possible frozen state of landscapes, especially in tundra (e.g., frozen water in troughs). Horizontal accuracy is also an important characteristic of LiDAR elevation data [*Hodgson and Bresnahan*, 2004]. Horizontal inaccuracy is usually larger than vertical inaccuracy (~two times that of vertical accuracy) and highly controlled by the vertical accuracy, in which very high vertical accuracies essentially have to be accompanied by very high horizontal accuracy. This is primarily because horizontal inaccuracies contribute significantly to computations of vertical accuracies [*ASPRS*, 2004; *Hodgson and Bresnahan*, 2004].

3.2.2. Relative Error

Because the surface morphometry represented by LiDAR data is internally consistent (spatially autocorrelated) [*Gangodagamage et al*., 2008], the DEM-derived products such as slope, curvature, and aspect are much more accurate than the absolute accuracies represented by the LiDAR elevation data. For example, the topographic slope derived from LiDAR data is partially independent from the absolute elevations, because the derivative of the elevation is dependent on the internal consistency of the data points. The point-to-point or relative vertical error is more important for derivative products (e.g., slope—first-order derivatives; curvature—second-order derivative) than the absolute vertical accuracy, and it only utilizes local differences among the adjacent elevation values of LiDAR elevation data [*ASPRS*, 2004].

We used the 284 DGPS elevation points and their corresponding LiDAR elevation to assess the relative error in elevation values of LiDAR DEM. We then used this vertical relative error to compute relative errors in LiDAR-derived products such as slopes, curvature, *DD*, and *NDD*. We computed the point-wise relative

differences in elevations for the DGPS points and point-wise relative differences for LiDAR data separately. First, we considered LiDAR elevation points (284 points). The first-order differences from each LiDAR point ($\Delta h_{LiDAR}(i)$) to all other LiDAR points were computed, and then the same approach was repeated to compute the first-order differences in DGPS points ($\Delta h_{DGPS}(i)$) as well. This procedure was carried out for all 284 points ($i = 1{:}284$), and their differences were computed as follows:

$$\Delta h_i(i=1:n)=\sqrt{\left(\frac{1}{(n+1-i)}\sum_{j=i}^{n}\left\{[h_{LiDAR}(i)-h_{LiDAR}(j)]-[h_{DGPS}(i)-h_{DGPS}(j)]\right\}^2\right)} \tag{3}$$

Here, $\Delta h_i(i = 1{:}n)$ are the relative elevation differences in LiDAR and DGPS points where i varies from point 1 to 284, $h_{LiDAR}(i)$ is the LiDAR elevation at point i, and $h_{LiDAR}(j)$ is the LiDAR elevation at point j, with j varying from 1 to 284, and j always equal to or larger than i. Here, $h_{DGPS}(i)$ is the DGPS elevation at point i, $h_{DGPS}(j)$ is the DGPS elevation at point j, and n ($n = 284$) is the total number of points used for the analysis. Then, we computed the average relative error in elevation (δ_a) by taking the mean value of the elevation difference associated with each point as:

$$\delta_a=\frac{1}{n}\sum_{i=1}^{n}(\Delta h_i(i)) \tag{4}$$

In relative error computation, we considered only vertical elevation differences between points; no horizontal distances between points were considered. We assumed that the relative horizontal error (δ_b) in LiDAR data is two times that of the vertical error, $\delta_b = 2 \times \delta_a$, while the absolute horizontal errors of LiDAR are approximately equal or less than two times of the vertical errors [*ASPRS*, 2004]. We assumed that the same error ratio exists between relative vertical errors and relative horizontal errors. We considered slope (s) as the ratio of rise (height in vertical axis, a) over run (distance in horizontal axis, b). The accuracy of the slope is determined by both vertical accuracies and horizontal accuracies. The relative error in vertical elevations is denoted as δ_a; the relative error in horizontal distances δ_b. The error in slope is considered as δ_s. Estimated uncertainty in the vertical direction is $a \pm \delta_a$, estimated uncertainty in the horizontal direction is $b \pm \delta_b$, and estimated uncertainty in slope is $s \pm \delta_s$. Error in the uncertainty of slope (δ_s) can be expressed as (see Appendix A for details, equation (A4)):

$$\delta_s=\frac{\delta_a}{b}+s\frac{\delta_b}{b} \tag{5}$$

The same derivation can be used to derive the relative error in curvature, by considering curvature as the rate of change in slope for each pixel. Change in slope for a pixel is considered as c, and relative error associated with curvature is assumed as δ_c, which can be expressed as:

$$\delta_c=\frac{\delta_s}{b}+c\frac{\delta_b}{b} \tag{6}$$

Finally, it can be shown that the relative error of the *DD*, δ_{DD}, is equivalent to the relative horizontal error, δ_b. The relative error of the *NDD*, δ_{NDD}, is equivalent to $2\delta_b$ (Appendix A).

3.3. Regression Model Development

We developed a simple piecewise multivariate-linear-regression model to predict the response variable *ALT* using normalized *DD* (*NDD*), *S*, *WC*, and *NDVI* as

$$ALT_i=a_i+b_i(NDD)+c_i(S)+d_i(WC)+e_i(NDVI)+n_i \tag{7}$$

where $a_i, b_i, c_i, d_i,$ and e_i are the piecewise regression coefficients, and n_i is the error term obtained for $i = 1{:}3$ cases that were derived from the three zones defined by directed distance. *NDD* is defined as

$$NDD_i=\frac{DD_i-\min(DD)_i}{\max(DD)_i-\min(DD)_i} \tag{8}$$

Table 1. The Distribution of *ALT* Point Measurements Over Different Microtopographic Zones Is Given

	Total Points	Main Transect	Side Transects	Main Transect: Detailed Sites DS1, DS2, and DS3	Site B and Site C
Sampling interval (m)		3	25	0.5	0.5
Total points	407	158	42	99	108
Zone 1 (Rims (LC) + elevated centers (HC))	145	48	14	36	47
Zone 2 (Centers (LC))	98	42	10	27	19
Zone 3 (Trough LC/HC)	165	68	18	37	42

where DD_i is the flow path distance of a pixel at Zone *i* and *i* represents $i = 1$, 2, or 3; $min(DD)_i$ is the minimum *DD* value in Zone *i*; and $max(DD)_i$ is the maximum value of the *DD* in Zone *i*.

We used a uniform sampling approach to obtain 407 *ALT* measurements (Table 1), employing a 25 m sampling interval to collect *ALT* points (42 measurements) along two outside transects (Figure 1) and a 3 m sampling interval for the *ALT* measurements along the center transect (158 measurements; Figure 1). A 0.5 m sampling interval was used within detailed sampling sites (i.e., DS1, DS2, and DS3; 99 measurements) and Site B and Site C (108 measurements; Table 1).

A total of 407 *ALT* measurements were used for model development (Figure 1): 262 measurements were used in model training and the remaining 145 measurements were used for model validation. Among these *ALT* measurements, 89, 66, and 108 points were used for model training and 56, 32, and 57 points were used for model validation in Zone 1, Zone 2, and Zone 3, respectively. The distribution of microtopographic types in each zone are given in Table 2.

Model uncertainty was evaluated using a coefficient of determination (r^2), and model error was evaluated using analyses of residuals for Mean Average Error (MAE), Mean Bias Error (MBE), Root Mean Squared Error (RMSE), and Willmott's index of agreement (d) [*Willmott*, 1981, 1982; *Willmott and Matsuura*, 2005]. Systematic and unsystematic RMSE (i.e., $RMSE_s$ and $RMSE_{us}$) were also evaluated, both for training and validation data sets separately.

Relative uncertainties of predicted *ALTs* at each pixel location were also computed as ratio between uncertainties in *ALT* and absolute predicted *ALT* value at that pixel location. Uncertainty therein was estimated as deviation from the corresponding mean values considering their microtographic zonations:

$$Relative\ \ Uncertainty_{ALT} = \frac{ALT_{p,z_i} - <ALT>_{z_i}}{ALT_{p,z_i}} \tag{9}$$

where ALT_{p,z_i} is the value of the predicted *ALT* in Zone i, Here $i = 1$, 2, or 3 and $<ALT_{p,z_i}>$ is the mean *ALT* value in Zone *i*.

We developed three regression models representing three microtopographic classes: Zone 1, Zone 2, and Zone 3. For each multiple regression, *ALT* samples were chosen to represent Zone 1, Zone 2, and Zone 3, such that sample sizes satisfy the likelihood (probability) of obtaining a significant ($p < 0.05$) r^2. To satisfy the above statistical power criteria in the regression, the minimum sample size was 50 [*Cohen and Cohen*, 1983; *Cohen*, 1988; *Cohen et al.*, 2003; *Thompson*, 2012]. The sample size we used in each of three regression models was

Table 2. Distribution of *ALT* Points Chosen from Three Different Microtopography Classes for Training and Validation in Piecewise Regression Model Is Given

	Training				Validation			
Descriptions	Total Number of *ALT*	Main Transect	Main Transect (DS1, DS2, and DS3)	Site B and Site C	Total Number of *ALT*	Side Transects	Main Transect (DS1, DS2, and DS3)	Site B and Site C
Total points	262	158	50	54	145	42	49	54
Zone 1 (Rims (LC) + elevated centers (HC))	89	48	18	23	56	14	18	24
Zone 2 (Centers (LC))	66	42	14	10	32	10	13	9
Zone 3 (Trough LC/HC)	108	68	19	21	57	18	18	21

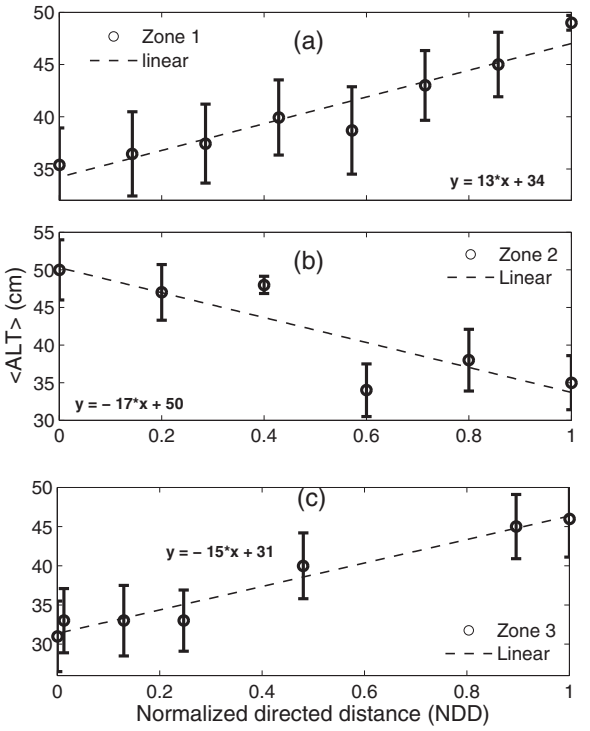

Figure 5. Ensemble averaged *ALT* (±1 std; <*ALT*>) distribution as a function of *DD* in (a) Zone 1 ($0 \leq DD \leq 7$), (b) Zone 2 ($7 < DD \leq 15$), and (c) Zone 3 ($DD > 15$) regions.

larger than 66 (Table 2), which was larger than the preferred sample size as defined in the above statistical power relationship [*Cohen and Cohen*, 1983; *Cohen*, 1988]. The sample sizes used in our study also were cross-checked with the conventional tools generally used for quantifying the adequacy of sample size in regression model development. The rule proposed by *Stevens* [2002] and *Park and Dudycha* [1974] suggested using 15 measurements for each explanatory variable (ratio of 15:1). We used four variables and the preferred sample size derived from this method (60 samples). The minimum sample size in this study (i.e., 66) was larger than the preferred sample size (i.e., 60) obtained from the traditional method.

4. Results

4.1. Relationships Between *ALT* and Surface Parameters

A shaded relief map of HC and LC polygons is shown in Figure 3a, and a classified LiDAR elevation map for three micropotopographic regions (i.e., Zone 1, Zone 2, and Zone 3) is shown in Figure 3b [Gangodagamage and Wullschleger 2014a, 2014b]. Two peaks in *ALT* were observed when *ALT* values were plotted against directed distance (Figure 4). The first peak occurred at a *DD* of approximately 3 m, associated with the locations of troughs. The second and largest *ALT* peak was located at a *DD* of approximately 7 m, which corresponds to the distance between the rim and the LC polygon center (Figure 2). The three zones we used for the regression model development are shown in Figure 4.

We observed a systematic shift in the relationship between *DD* and *ALT* in the three zones (Figure 5). Accordingly, regression relationships were developed for each zone. In Zone 1, which represents the elevated polygon centers (HC polygons) and rims (LC polygons), *ALT* has a positive correlation with *DD* with the thaw depths increasing as one moves away from the elevated mounds (center or rim; Figure 5a). A decreasing trend in *ALT* was observed in Zone 2, i.e., a reduced *ALT* as one moves from the LC polygon center toward the trough (Figure 5b). The *ALT* increases with *DD* in Zone 3, suggesting a deepening of the active layer in the troughs compared to the edges of the HC polygon mound and the elevated LC polygon rims. However, the rate was an order of magnitude lower in Zone 3 than observed in Zone 1 (Figure 5c).

Figures 6a–6c show the *ALT* as a function of local slope. Across all three zones, there was a negative correlation between slope and *ALT*, and this trend increased from Zone 1 (220 cm per m/m) to Zone 3 (360 cm per m/m). All three zones showed a statistically significant ($p < 0.05$) relationship between *ALT* and slope. The highest correlation between slope and *ALT* was observed in Zone 3 (Figure 6c), whereas the lowest correlation was observed in Zone 1 (Figure 6a). All zones showed an increase in *ALT* as curvature increased (Figures 7a–7c). Across the study area, we observed a positive correlation between *NDVI* and *ALT* (Figure 8), with the *NDVI* values ranging from 0.48 to 0.51. In Zone 1, *NDVI* values were representative of the vegetation conditions, whereas in Zone 2 and Zone 3, *NDVI* values were more representative of soil moisture and inundation conditions.

The most important contribution to error in our analysis is the relative vertical error (point-to-point accuracy), because the topographic variables we used in this work are the first derivatives of the elevation (slope) and the second derivatives of the elevation (curvature). The relative vertical error of the LiDAR

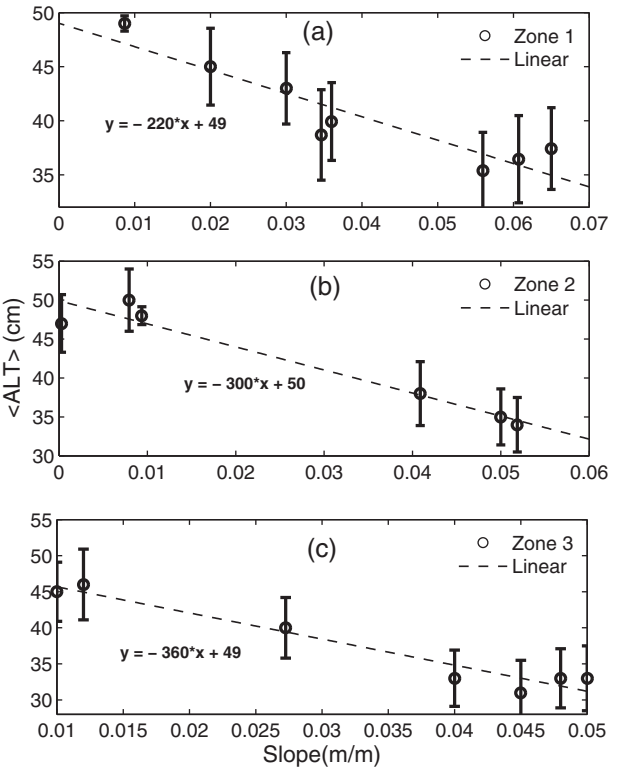

Figure 6. Ensemble averaged *ALT* ($\pm$1 std; $<ALT>$) distribution as a function of slope is given in (a) Zone 1 ($0 \leq DD \leq 7$), (b) Zone 2 ($7 < DD \leq 15$), and (c) Zone 3 ($DD > 15$) regions.

elevation data set was 0.0014 m (equations (3)–(6)). The same approach was used to compute the relative vertical errors in three microtopographic classes used in this study. Zone 1 showed 0.001 m relative vertical error, whereas Zone 2 and Zone 3 showed 0.0016 and 0.0020 m relative vertical errors, respectively.

We also tested how the accuracy of LiDAR elevation data set propagate into LiDAR-derived slope, curvature, *DD*, and *NDD*. The effect of the elevation error on slope was quantified using equation (5). The computed relative accuracy in slope was 0.004 m/m ($\sim$0.004°) for the maximum slope value (i.e., 0.07 $\pm$ 0.004 m/m; $p < 0.05$). We also computed the relative error in slope of Zone 1, Zone 2, and Zone 3 separately: Zone 1 was 0.005 m/m (0.005°) whereas slopes in Zone 2 and Zone 3 were 0.003 m/m (0.003°) and 0.004 m/m (0.004°; $p < 0.05$). We used the same approach to compute the relative error in curvature by considering the curvature as the rate of change in slope for each pixel of the elevation data. This approach resulted in a relative error of curvature of 0.01 1/m for the maximum curvature of 0.04 (0.04 $\pm$ 0.01 1/m). The relative error of *DD* was 0.0028 m, and the relative error of *NDD* was 0.0056 m.

4.2. *ALT* Prediction

Based on the methodology outlined in section 2 above, we computed the coefficients in regression (equation (7)) for the each of three zones. Using the piecewise regression model, we predicted *ALT* values across a 5 km^2 area (shown only for a 0.15 km^2 subset from the 5 km^2 for better microtopographic feature representation) for which the LiDAR elevation data were available (Figure 10b). The r^2 of the regression model was 0.76 (p value < 0.001, RMSE 4.2 cm, and MAE 3.7 cm). The $RMSE_s$ was 2.24 cm, and $RMSE_{us}$ was 3.63 cm. The percentage of $RMSE_s$ was 27%, and the $RMSE_{un}$ was 73% of the overall RMSE. The MAE and MBE were 3.54 and -0.87, respectively, for the training data set.

The model predicted *ALT* values between 20 and 70 cm, while the respective field measurements ranged from 22 to 58 cm. Lower *ALT* values were predicted for the HC polygons and rims of LC polygons, while higher *ALT* values were predicted for troughs and the center areas of the LC polygons (Figure 10b).

The model successfully predicted both the magnitude and variability in a spatially coherent way, without major systematic bias (Figure 9a). Overall r^2 between training and predicted values along the transect, site-B, and site-C was 0.81 (p value 0.003; Figure 9b2). MAE and MBE were 3.54 and -0.87. RMSE was 3.99 cm, and $RMSE_s$ and $RMSE_{us}$ were 2.17 cm and was 3.35 cm, which were 24% and 76% from the overall RMSE, respectively. No major systematic spatial error in the model was observed in either the training or validation data sets, and errors were mainly associated with random noise. The highest correlated variable with *ALT* was slope; the lowest correlated variable was *NDVI*. We also compared the predictive power of all the parameters in *ALT* predictions and found that the partial covariance of slope was 158% higher than *DD*. Further, the correlation between DD and ALT is 144% and 121% higher than that of the NDVI and curvature with the ALT.

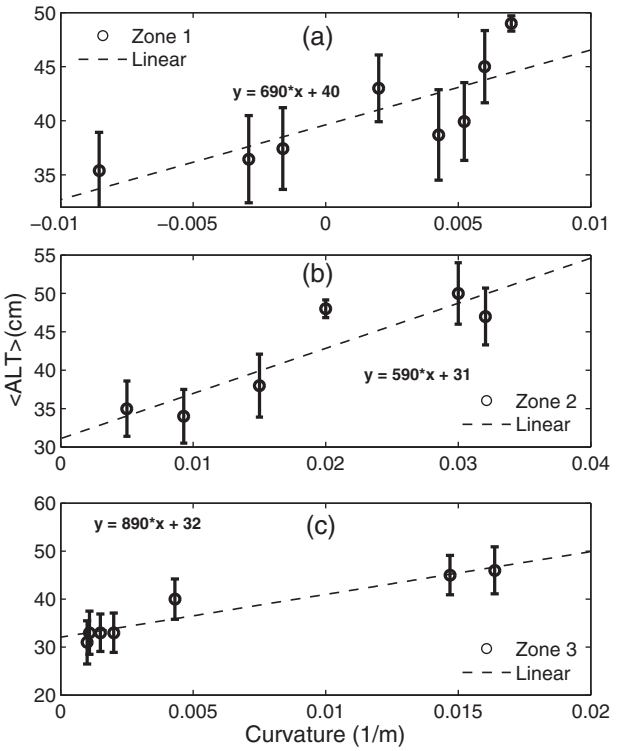

Figure 7. Ensemble averaged *ALT* (±1 std; <*ALT*>) distribution as a function of curvature is given in (a) Zone 1 ($0 \leq DD \leq 7$), (b) Zone 2 ($7 < DD \leq 15$), and (c) Zone 3 ($DD > 15$) regions.

The highest relative uncertainty (mean uncertainty 1.3%, standard deviation 12%, maximum <12%) in predicted *ALT* was shown by Zone 3 (polygons centers), whereas the lowest uncertainty (mean uncertainty 1%, standard deviation 10%, maximum <44%) was shown by Zone 1 (rims and elevated ridges; Figure 10).

5. Discussion

ALT is fundamentally a function of the warming experienced by the soil and subsurface. At regional scales, broad patterns in *ALT* correspond to mean annual air temperatures, with warmer regions having greater *ALT*s [*Romanovsky et al*., 2002; *Jorgenson et al*., 2001]. Vegetation and snow cover, organic and mineral composition of soils, and soil moisture content all influence the transfer of heat from the atmosphere into the ground [*Romanovsky and Osterkamp*, 1995]. These attributes vary both in time and space, and the thermal conductivity of the ground depends both on the total water content and the phase of the water [*Burn and Smith*, 1998; *Smith and Riseborough*, 2002]. Because these properties, as well as topography, vary at small scales (1–100 m), *ALT* may show significant local deviations from regional averages. For example, in Barrow, Alaska, a continuous time series of annual *ALT* records from 1994 to 2009 at the nearby CALM site (700 m east and 3500 m north of our study site) demonstrated significant variation in *ALT* among different landcape types, including beach ridges, drained lake basins, and polygonal uplands [*Shiklomanov et al*., 2010]. They found that *ALT* in beach ridges was 20 cm greater than that of polygonal uplands. Drained lake basins also showed on average 5 cm deeper *ALT*s than polygonal uplands. Thinner *ALT* values were documented in areas south and southwest of Barrow, on the Arctic coastal plain [*Nelson et al*., 1998].

Because the transfer of heat from the atmosphere into the subsurface is so strongly controlled by local surface and subsurface properties, no relationship between a deepening of *ALT* and observed climatic warming has been universally documented. In northern Mackenzie basin, NWT, *ALT* has shown a clear increase from 42 to 50 cm from 1998 to 2008 [*Burn and Kokelj*, 2009]. *Burn and Kokelj* [2009] also observed an increase in permafrost temperature of approximately 0.1°C per year from 1990 to 2000 at a depth of 28 m. In contrast, permafrost temperatures at the same location in Barrow warmed by 1°C at 15 m depth between 9 October 1950 and 9 October 2001. However, despite this warming, no associated trends in *ALT* were observed [*Romanovsky et al*., 2002] until 2005. The lack of global trends between *ALT* and permafrost temperature suggest local eco-hydro-geomorphology may play a significant role in *ALT* spatial distributions [*Shiklomanov et al*., 2010]. In this context, it is highly important to understand the complex interactions of microtopography, vegetation, soil moisture, etc., on *ALT* distributions at submeter scales.

In this study, we developed a piecewise regression model representing three microtopographic zones for *ALT* estimations. These zones (Zones 1, 2, and 3) were delineated using the microtopographic positions of polygonal features (quantified by directed distance) and associated *ALT* measurements (Figure 4). We

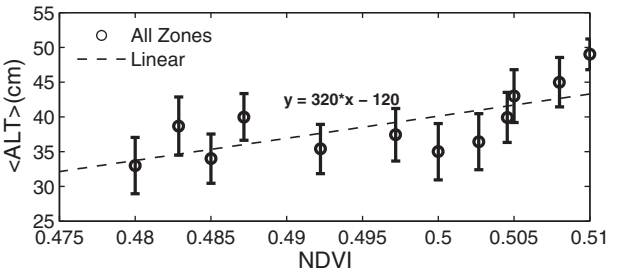

Figure 8. Ensemble averaged *ALT* (±1 std; <*ALT*>) distribution as a function of *NDVI* is given in for all Zones (i.e., Zone 1 ($0 \leq DD \leq 7$), Zone 2 ($7 < DD \leq 15$), and Zone 3 ($DD > 15$)). Low *NDVI* values are associated with elevated centers and rims in HC and low centered polygons.

hypothesized that these observed zones reflect the geo-hydro-thermal regimes controlled by geomorphic attributes in combination with soil moisture, water storage, and vegetation conditions. Previous studies in polygonal landscapes have documented that the zonations we observed here have unique geo-hydro-thermal process controls [*Gamon et al.*, 2012; *Liljedahl et al.*, 2012; *Zona et al.*, 2011; *Bockheim et al.*, 1999; *Hinzman and Kane*, 1991; *Pavlov*, 1975; *Nelson et al.*, 1997; *Hinzman et al.*, 1998; *Shiklomanov and Nelson*, 1999], but few studies have attempted to isolate geomorphic influences on *ALT* at finer scales [*Minke et al.*, 2009]. We used LiDAR-derived topographic slope, curvature, and *NDD* as well as *NDVI* (a surrogate variable for vegetation and soil moisture variability) to capture the influence of local geomorphology, vegetation, water storage, and soil moisture on *ALT*. We specifically applied the regression model for three zones separately, and estimated model parameters unique to each zone. Low *NDD* values in Zone 1 were associated with the elevated centers and rims where low *ALT* values were observed. Because lower *NDD* values in Zone 1 were associated with low flow accumulations, high slope conditions, and high runoff conditions, this zone is well drained and has low water storage, deeper water tables, and low soil moisture conditions [*Liljedahl et al.*, 2012; *Hinzman and Kane*, 1991; *Pavlov*, 1975]. Zone 1 is primarily a divergent landscape that warms quickly during the day and cools rapidly at night; as such, a lower heat transfer into deeper soil layers can be expected. Furthermore, because the vegetation in Zone 1 has higher albedo [*Gamon et al.*, 2012], less heat is available to transfer into deeper soil layers. When low heat fluxes are accompanied by low moisture conditions, active layer development is limited to shallow depths [*Minke et al.*, 2009], resulting in lower *ALT* values in Zone 1.

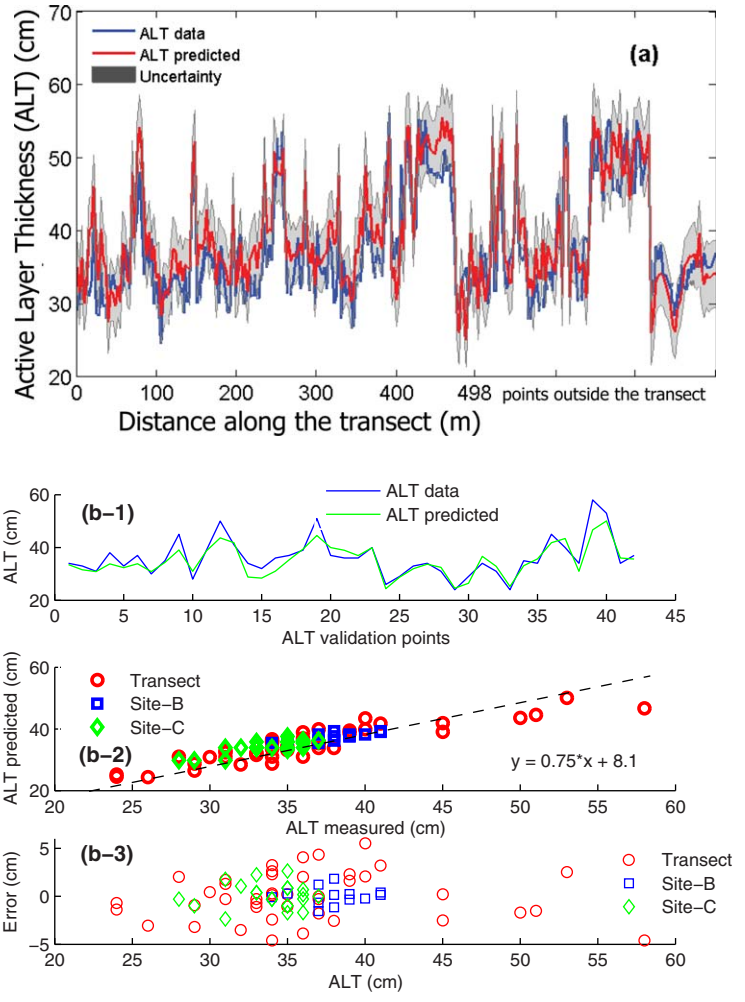

Figure 9. (a) Predicted *ALT* plotted along the measurements obtained along a geophysical transect. (b1) *ALT* predicted values at the calibration points are shown (green) and the measured values are shown (blue). (b2) Measured thaw-depths values at three validation sites (transect, Zone B, and Zone C) in relation to predicted *ALT* values. (b3) Error associated with measured and predicted *ALT* values at the validation sites.

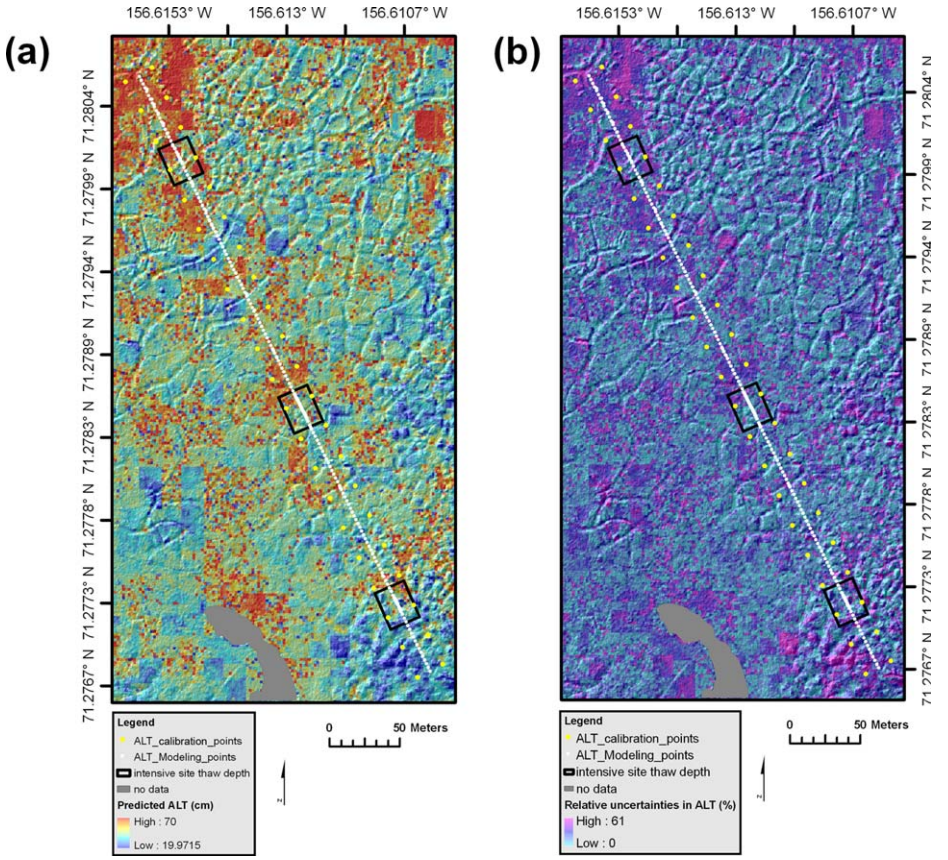

Figure 10. (a) *ALT* for a ~300 × 500 m^2 of the study area, predicted using a data fusion approach adapted for use with data from remotely sensed measurements, showing the geophysical transect location (yellow line), and the location of additional *ALT* measurements on either side of the transect. (b) The relative uncertainty of the *ALT* measurement computed separately considering their microtopographic zonations (i.e., Zone 1, Zone 2, and Zone 3).

In Zones 2 and 3, areas of lower slopes and positive (concave) curvatures lead to greater water storage. Areas of positive curvature in these zones showed deeper *ALT* values than in areas of negative curvature in Zone 1 (Figures 7a–7c). The concave areas are associated with greater ground heat flux, resulting from high water and moisture availability [*Shiklomanov et al*., 2010; *Zona et al*., 2011]. Furthermore, concave areas in Zone 2 and Zone 3 tend to pond water and retain soil moisture, as opposed to convex areas in Zone 1 that more readily drain. Ponded waters and higher soil moisture in Zone 2 and Zone 3 likely lead to enhanced conductive transfer of heat into subsurface layers, resulting in higher *ALT*s (Figures 6b, 6c, 7b, and 7c). Furthermore, lateral flows of organic matter transferred through wind and surface-water runoff [*Zona et al*., 2011] into low-slope, concave portions of the landscape may help promote the thicker organic layers observed in Zone 2 and Zone 3 [*Bockheim et al*., 1999]. These thicker organic layers help retain soil moisture and high moisture conditions can increase the heat conductance into deeper layers [*Hinzman and Kane*, 1991; *Pavlov*, 1975; *Williams and Smith*, 1989], promoting deeper *ALT*s in Zone 2 and Zone 3.

Analysis of *NDVI* data suggest that vegetation caused *NDVI* values to vary from 0.32 to 0.48 across different polygon morphologies. Lower *NDVI* values were associated with Zone 1 and higher *NDVI* values were associated with Zone 2 and Zone 3. Furthermore, *NDVI* values inversely correspond with the *ALT* values (thinner ALT for lower NDVI values; Figure 8). It is also possible that *NDVI* values in this polygon landscape represent not only vegetation condition, but also soil moisture conditions and inundations. For example, in the regression model for Zone 1, *NDVI* represents vegetation conditions, whereas in Zone 2 and Zone 3, *NDVI* potentially represents moisture conditions as well. Because each zone has a unique regression-model representation, our approach can yield a different parameterization for the same explanatory variable in different zones.

The highest uncertainty in the *ALT* predictions was associated with Zone 2 (center areas), whereas the lowest uncertainty was associated with Zone 1 (rims and elevated center areas). Our results suggest that Zone 1, representing topographic highs, has a lower *ALT* compared to Zones 2 and 3 (centers areas and troughs of LC polygons) representing wet topographic low areas. This is primarily because of the differences in albedo, soil moisture, vegetation, and polygon morphology in ice wedge polygon dominated tundra environments. If this field campaign were conducted in the first half of the the thaw season, it might be possible to see deeper thaw depths in the HC polygons, because thawing could be much faster in HC polygons compared to LC polygons. The greater energy in HC polygons would transfer more directly as conductive heat transfer than latent heat of fusion.

LiDAR data maintain higher levels of relative vertical accuracies than absolute accuracies, and these accuracies can change with different microtopographic types. In this work, we also introduced a simple approach to compute the relative vertical errors of LiDAR elevation data, using which we showed that how these errors propagate into LiDAR-derived topographic attributes like slope, curvature, and directed distance. These relative errors can be useful in understanding model uncertainties that arise when input data contain LiDAR-derived attributes. In future studies, we recommend the collection of more *ALT* measurements of center areas (LC polygons) and troughs than of rims (LC polygons) and elevated center areas (HC polygons) of the ice wedge polygon features.

The *ALT* prediction method we investigated in this work can be applied to other parts of the tundra, where *ALT* is primary controlled by microtopography, vegetation, and soil moisture, and where LiDAR and WorldView-2 data available. WorldView-2 data and LiDAR data are becoming increasingly available for this region (e.g., USGS has acquired LiDAR data along the Arctic coastal belt—personal communication with Ann Gibbs USGS Pacific Coastal and Marine Center, Santa Cruz, CA). In other Arctic environments, where polygons are not present, it is essential to calibrate the model parameters with proper site-specific *ALT* measurements. For example, the spatial distribution of *ALT* in Barrow is highly dependent on the microtopographic variability introduced by the ice-wedge formation. For the landscapes where ice wedges are not the primary control, *ALT* depends on topographic position [*Nelson et al*., 1997]. In hilly environments, particularly in Arctic foothills, *ALT* depends on topographic positions from the top of a hillslope to the valley and channel floodplains. The topographic attributes (slope, curvature, and directed distance) used in this study can be effectively used to characterize the topographic position in hillslopes [*Gangodagamage et al*., 2011]. The models proposed in this work could work well for environments where microtopography primarily consists of features such as found in our Zone 1, Zone 2, and Zone 3. If this model is used in landscapes where the microtopographic features, surface, atmospheric, and subsurface dynamics are different, the model needs to be redeveloped using region specific data sets, which will possibly provide better generalizations for *ALT* variability for that area.

We used the regression equation to predict the *ALT* using three regression models representing three microtopographic classes (i.e., Zone 1, Zone 2, and Zone 3). The sample sizes we used satisfy both the likelihood (probability) of obtaining a significant ($p < 0.05$) and r^2. Traditional rules like statistical significance do not provide insights about statistical power [*Asher*, 1993]. Statistical significance itself may be obtained from a large enough sample size, even though there is very little relationship between the dependent and explanatory variables [*Asher*, 1993]. It is important when developing predictive regression models, the sample sizes to be chosen so as to provide both statistical significance and statistical power, which then can be expected to yield better generalization of the model beyond the samples used to develop the model.

6. Conclusions

Current methods are very good at quantifying and predicting *ALT* at either local or regional scales. No method has been presented that is able to capture both the fine scale variation in *ALT* related to the microtopography of rims, troughs, and centers in ice wedge polygon landscapes, and the influence of microtopography on *ALT* over large spatial domains. Our results indicate that it is possible to predict *ALT* with a high level of accuracy at high spatial resolution in a noninvasive

manner, using a combination of microtopographic and land-surface characteristics over large spatial domains.

It is generally accepted that *ALT* increases in response to climate warming [*Lawrence et al*., 2008], but how this increase is related to local topographic variability within and between polygons is still poorly quantified. The response of *ALT* to climate warming is likely to be complex and dependent on many parameters. As has been documented, the primary control of *ALT* at larger scales (~1 km or larger) is air temperature [*Zhang et al*., 1997; *Nelson et al*., 1997], which potentially controls the average *ALT* values at landscape scale. *Jorgenson et al*. [2010] have found correlations between *ALT* and hillslope position, *Zona et al*. [2011] showed that *ALT* varies with polygon microtopography, and *Minke et al*. [2009] have observed that shallower thaw depths were associated with higher microrelief regions of LC polygons. In this study, we found that local variables, including the heterogeneity of soil moisture, water ponding, and vegetation conditions (all quantified by *NDVI*)—as well as geomorphic attributes quantified by slope, curvature, and *NDD*—play a significant role in small-scale (~2 m) *ALT* variations. Consistent with previous studies, our study suggests that while broad climatic variability associated with warming will govern the regional averages of *ALT*, the smaller-scale variability of *ALT* is controlled by the aforementioned local geomorphic, hydrological, and vegetation variables.

Furthermore, this study suggests the importance of developing techniques to better landscape characterization, and the importance of identifying the process-based microtopographic zones that mainly govern the spatial distribution of *ALT*s. Our approaches enabled spatially classified process-based zones to capture complex geohydrothermal interactions using simple linear representations, among model variables controlling the spatial variability of *ALT*s. While our model does require local data for the calibration of the metrics, it should be widely applicable to polygonal terrains outside the Barrow, AK. This applicability arises from the hydrological, thermal, and geomorphic controls *ALT* captured via the landscape metric used in our model.

Appendix A

Provided herein is the derivation of relative errors for slope and curvature. Slope is the ratio of rise (height in vertical axis, a) over run (distance in horizontal axis, b). The accuracy of the slope is determined by both vertical accuracies and horizontal accuracies. Relative error in vertical accuracy is δ_a; relative error in horizontal accuracy δ_b. The error in slope is considered as δ_s. Estimated uncertainty in the vertical direction is $a \pm \delta_a$, estimated uncertainty in the horizontal direction is $b \pm \delta_b$, and estimated uncertainty in slope is $s \pm \delta_s$.

Consider the quotient for slope:

$$s \pm \delta_s = \frac{a \pm \delta_a}{b \pm \delta_b} \tag{A1}$$

The maximum slopes can be obtained as:

$$Max(s) = s + \delta_s = \frac{a + \delta_a}{b - \delta_b} \tag{A2}$$

This equation can be written as:

$$a + \delta_a = (s + \delta_s)(b - \delta_b) = sb - s\delta_b + b\delta_s - \delta_s\delta_b = a - s\delta_b + b\delta_s \tag{A3}$$

where the term $\delta_s\, \delta_b$ has been neglected in the equation and the relationship, $sb = a$, is considered. This can be rearranged as:

$$\delta_s = \frac{\delta_a}{b} + s\frac{\delta_b}{b} \tag{A4}$$

The same derivation can be used to derive the error in accuracy of curvature, by considering curvature as the rate of change in slope for each pixel. Change in slope for a pixel is considered *c*, and error in accuracy associated with curvature is assumed to be δ_c, which can be expressed as:

$$\delta_c = \frac{\delta_s}{b} + c\frac{\delta_b}{b} \tag{A5}$$

The same way the accuracy of the *DD*, δ_{DD}, is equivalent to the horizontal accuracy, δ_b. The accuracy of the *NDD*, δ_{NDD}:

$$\delta_{NDD} = 2\delta_b \tag{A6}$$

Acknowledgments
This project was funded by the Next-Generation Ecosystem Experiments Arctic (NGEE-Arctic) project, which is supported by the Director, Office of Science, Office of Biological and Environmental Research of the U.S. Department of Energy under contract DE-AC02-05CH11231. Authors would like to thanks the three anonymous reviewers for their helpful comments. Helpful discussions with Jacques Cloutier from Aero-Metric, Inc. Anchorage, AK are greatly appreciated.

References

Asher, W. (1993), The Role of statistics in research, *J. Exp. Educ.*, *61*(4), 388–393.

ASPRS (2004), *Vertical Accuracy Reporting for LiDAR Data*, Am. Soc. for Photogramm. and Remote Sens., LiDAR Comm., Bethesda, Md. [Available at http://www.asprs.org/a/society/committees/lidar/Downloads/Vertical_Accuracy_Reporting_for_Lidar_Data.pdf, last accessed Dec. 2013.]

Babb, T. A., and D. W. A. Whitfield (1977), Mineral nutrient cycling and limitation of plant growth in the Truelove Lowland ecosystems, in *Truelove Lowland, Devon Island, Canada: A High Arctic Ecosystem*, edited by L. C. Bliss, pp. 587–606, Univ. of Alberta Press, Edmonton, Canada.

Berk, R. (2008), *Statistical Learning From a Regression Perspective*, 360 pp., Springer, Berlin.

Bliss, L. C., and K. M. Peterson (1992), *Plant Succession, Competition, and the Physiological Constraints of Species in the Arctic*, 111–136, Academic, N. Y.

Bockheim, J. G., L. R. Everett, K. M. Hinkel, F. E. Nelson, and J. Brown (1999), Soil organic carbon storage and distribution in Arctic Tundra, Barrow, Alaska, *Soil Sci. Soc. Am. J.*, *63*, 934–940, doi:10.2136/sssaj1999.634934x.

Brewer, M. C. (1958), Some results of geothermal investigations of permafrost in northern Alaska, *Trans. AGU*, *39*(1), 19–26, doi:10.1029/TR039i001p00019.

Britton, M. E. (1957), Vegetation of the arctic tundra, in *Arctic Biology*, edited by H. P. Hanson, pp. 67–130, Oreg. State Univ. Press, Corvallis.

Brown, J., P. C. Miller, L. L. Tieszen, and F. Bunnell (1980), *An Arctic Ecosystem: The Coastal Tundra at Barrow*, 616 pp., Dowden Hutchinson Ross, Stroudsburg, Pa.

Brown, J., K. M. Hinkel, and F. E. Nelson (2000), The circumpolar active layer monitoring (CALM) program: Research designs and initial results, *Polar Geogr.*, *24*(3), 165–258, doi:10.1080/10889370009377698.

Burn, C., and C. Smith (1988), Observations of the "thermal offset" in near-surface mean annual ground temperatures at several sites near Mayo, Yukon Territory, Canada, *Arctic*, *41*(2), 99–104, doi:10.14430/1700.

Burn, C. R., and S. V. Kokelj (2009), The environment and permafrost of the Mackenzie delta area, *Permafrost Periglacial Processes*, *20*, 83–105, doi:10.1002/ppp.655.

Chapin, F. S., N. Fetcher, K. Kielland, K. R. Everett, and A. E. Linkins (1988), Productivity and nutrient cycling of Alaskan tundra: Enhancement by flowing soil-water, *Ecology*, *69*(3), 693–702, doi:10.2307/1941017.

Chapin, F. S., III, and K. Van Cleve (1978), Nitrogen and phosphorus distribution in an Alaskan tussock tundra ecosystem: Natural patterns and implications for development, in *Environmental Chemistry and Cycling Processes: Proceedings of Symposium*, *Augusta*, Georgia, edited by D. C. Adriano and I. L. Brisbin Jr., pp. 738–753, U.S. Dep. of Energy, Washington, D. C.

Cohen, J. (1988), *Statistical Power Analysis for the Behavioral Sciences*, 2nd ed., 559 pp., Lawrence Erlbaum, Hillsdale, N. J.

Cohen, J., and P. C. Cohen (1983), *Applied Multiple Regression/Correlation Analysis for the Behavioral Sciences*, 2nd ed., 580 pp., Lawrence Erlbaum, Hillsdale, N. J.

Cohen, J., P. C. Cohen, S. G. West, and L. S. Aiken (2003), *Applied Multiple Regression/Correlation Analysis for the Behavioral Sciences*, 3rd ed., 703 pp., Lawrence Erlbaum, Mahwah, N. J.

Drew, J. V. (1957), A pedologic study of arctic coastal plain soils near Point Barrow, Alaska, PhD dissertation, Rutgers Univ., New Brunswick, N. J.

French, D. O. (1974), Classification of IBP Tundra biome sites based on climate and soil properties, in *Soil Organisms and Decomposition in Tundra: Proceedings of the Microbiology, Decomposition and Invertebrate Working Groups Meeting, Fairbanks, Alaska*, pp. 3–25, edited by A. J. Holding et al., Int. Biol. Program., Tundra Biome Steering Comm., Stockholm, Sweden.

Gamon, J. A., G. P. Kershaw, S. Williamson, and D. Hik (2012), Microtopographic patterns in an arctic Baydjarakh field: Do fine-grain patterns enforce landscape stability? *Environ. Res. Lett.*, *7*, 015502, doi:10.1088/1748-9326/7/1/015502.

Gangodagamage, C., and S. Wullschleger (2014a), A digital map of the high center (HC) and low center (LC) polygon boundaries delineated from high resolution LiDAR data for Barrow, Alaska, doi:10.5440/1136188. [Available at http://www.osti.gov/scitech/servlets/purl/1136188.]

Gangodagamage, C., and S. Wullschleger (2014b), Microtopographic characterization of ice-wedge polygon landscape in Barrow, Alaska: a digital map of troughs, rims, centers Derived from high resolution (0.25 M) LiDAR data, doi:10.5440/1136189. [Available at http://www.osti.gov/scitech/servlets/purl/1136189.]

Gangodagamage, C., E. Barnes, and E. Foufoula-Georgiou (2007), Scaling in river corridor widths depicts organization in valley morphology, *Geomorphology*, *91*, 198–215, doi:10.1016/j.geomorph.2007.04.014.

Gangodagamage, C., C. X. Zhou, and H. S. Lin (2008), Spatial autocorrelation, in *Encyclopedia of GIS*, pp. 32–37, edited by S. Shekhar and H. Xiong, Springer, N. Y., doi:10.1007/978-0-387–35973-1_83. [Available at http://refworks.springer.com/geograph.]

Gangodagamage, C., P. Belmont, and E. Foufoula-Georgiou (2011), Revisiting scaling laws in river basins: New considerations across hillslope and fluvial regimes, *Water Resour. Res.*, *47*, W07508, doi:10.1029/2010WR009252.

Gersper, P. L., V. Alexander, S. A. Barkley, R. J. Barsdate, and P. S. Flint (1980), The soils and their nutrients, chap. 7, in *An Arctic Ecosystem, the Coastal Tundra at Barrow, Alaska, US/IBP Syn. Ser. 12*, edited by J. Brown et al., 571 pp., Dowden Hutchinson Ross, Stroudsburg, Pa.

Gooseff, M. N., A. Balser, W. B. Bowden, and J. B. Jones (2009), Effects of hillslope thermokarst in Northern Alaska, *Eos Trans. AGU*, *90*(4), 29–30, doi:10.1029/2009EO040001.
Harlan, R. L., and J. F. Nixon (1978), Ground thermal regime, in *Geotechnical Engineering for Cold Regions*, pp. 103–163, MacGraw-Hill, N. Y.
Hassol, S. J., et al. (2004), *Impacts of a Warming Arctic: Arctic Climate Impact Assessment*, Cambridge Univ. Press, Cambridge, U. K., doi: 10.2277/0521617782.
Hinkel, K. M., and F. E. Nelson (2003), Spatial and temporal patterns of active layer thickness at circumpolar active layer monitoring (CALM) sites in northern Alaska, 1995–2000, *J. Geophys. Res.*, *108*(D2), 8168, doi:10.1029/2001JD000927.
Hinzman, L. D., and D. L. Kane (1991), Snow hydrology of a headwater Arctic basin: 2. Conceptual analysis and computer modeling, *Water Resour. Res.*, *27*(6), 1111–1121, doi:10.1029/91WR00261.
Hinzman, L., D. Goering, and D. Kane (1998), A distributed thermal model for calculating soil temperature profiles and depth of thaw in permafrost regions, *J. Geophys. Res.*, *103*(D22), 28,975–28,991, doi:10.1029/98JD01731.
Hinzman, L. D., et al. (2005), Evidence and implications of recent climate change in northern Alaska and other arctic regions, *Clim. Change*, *72*(3), 251–298, doi:10.1007/s10584-005-5352-2.
Hodgson, M. E., and E. Bresnahan (2004), Accuracy of airborne LiDAR-derived elevation: Empirical assessment and error budget, *Photogramm. Eng. Remote Sens.*, *70*(3), 331–339.
Hodgson, M. E., J. Jensen, G. Raber, J. Tullis, B. A. Davis, G. Thompson, and K. Schuckman (2005), An evaluation of LiDAR-derived elevation and terrain slope in leaf-off condition, *Photogramm. Eng. Remote Sens.*, *71*(7), 817–823.
Hubbard, S. S, et al. (2013), Quanitifying and relating subsurface and land-surface variability in permafrost environments using surface geophysical and LiDAR datasets, *Hydrogeol. J.*, *21*, 149–169, doi:10.1007/s10040-012-0939-y.
IPCC (2013), *Climate Change 2013: The Physical Science Basis, Contribution of Working Group I to the Fifth Assessment Report of the Intergovernmental Panel on Climate Change*, Cambridge Univ. Press, Cambridge, U. K.
Jorgenson, M. T., C. H. Racine, J. C. Walters, and T. E. Osterkamp (2001), Permafrost degradation and ecological changes associated with a warming climate in Central Alaska, *Clim. Change*, *48*(4), 551–571, doi:10.1023/A:1005667424292.
Jorgenson, M. T, V. E. Romanovsky, J. Harden, Y. L. Shur, J. O'Donnell, T. Schuur, and M. Kanevskiy (2010), Resilience and vulnerability of permafrost to climate change, *Can. J. For. Res.*, *40*(7), 1219–1236, doi:10.1139/X10-060.
Koven, C. D., W. J. Riley, and A. Stern (2013), Analysis of permafrost thermal dynamics and response to climate change in the CMIP5 earth system models, *J. Clim.*, *26*, 1877–1900, doi:10.1175/JCLI-D-12-00228.1.
Lanardini, V. J. (1978), Theory of n-factors and correlations of data, in *Proceedings of 3rd International Conference on Permafrost*, vol. 1, pp. 40–46, Nat. Res. Counc. of Can., Ottawa, Ont.
Langer, M., S. Westermann, S. Muster, K. Piel, and J. Boike (2010), Permafrost and surface energy balance of a polygonal tundra site in northern Siberia part 1, Spring to fall, *Cryosphere Discuss.*, *4*(3), 901–947, doi:10.5194/tcd-4-901-2010.
Lashermes, B., E. Foufoula-Georgiou, and W. E. Dietrich (2007), Channel network extraction from high resolution topography using wavelets, *Geophys. Res. Lett.*, *34*, L23S04, doi:10.1029/2007GL031140.
Lawrence, D. M., A. G. Slater, V. E. Romanovsky, and D. J. Nicolsky (2008), Sensitivity of a model projection of near-surface permafrost degradation to soil column depth and representation of soil organic matter, *J. Geophys. Res.*, *113*, F02011, doi:10.1029/2007JF000883.
Liljedahl, A. K., L. D. Hinzman, Y. Harazono, D. Zona, C. Tweedie, R. D. Hollister, R. Engstrom, and W. C. Oechel (2011), Nonlinear controls on evapotranspiration in arctic coastal wetlands, *Biogeosciences*, *8*, 3375–3389, doi:10.5194/bg-8-3375-2011.
Liljedahl, A. K., L. D. Hinzman, and J. Schulla (2012), Ice-wedge polygon type controls low-gradient watershed-scale hydrology, in *Tenth International Conference on Permafrost, vol. 1: International Contributions*, pp. 231–236, edited by K. M. Hinkel, The Northern Publisher, Salekhard, Russia.
Liu, L., K. Schaefer, T. Zhang, and J. Wahr (2012), Estimating 1992–2000 average active layer thickness on the Alaskan North Slope from remotely sensed surface subsidence, *J. Geophys. Res.*, *117*, F01005, doi:10.1029/2011JF002041.
Lu, X., and Q. Zhuang (2012), Modeling methane emissions from the Alaskan Yukon River basin, 1986–2005, by coupling a large-scale hydrological model and a process-based methane model, *J. Geophys. Res.*, *117*, G02010, doi:10.1029/2011JG001843.
Mackay, J. R. (1973), A frost tube for the determination of freezing in the active layer above permafrost, *Can. Geotech. J.*, *10*(3), 392–396, doi:10.1139/t73-033.
Minke, M., N. Donner, N. Karpov, P. de Klerk, and H. Joosten (2009), Patterns in vegetation composition, surface height and thaw depth in polygon mires in the Yakutian Arctic (NE Siberia): A microtopographical characterization of the active layer, *Permafrost Periglacial Processes*, *20*(4), 357–368, doi:10.1002/ppp.663.
NCDC (2002), Climate of 2002 annual review significant U.S. and global events, Natl. Clim. Data Cent., Asheville, N. C. [Available at http://www.ncdc.noaa.gov/pubs/publications.html.]
Nelson, F. E., N. I. Shiklomanov, G. Mueller, D. Hinkel, K. M. Walker, and J. G. Bockheim (1997), Estimating active-layer thickness over a large region: Kuparuk River basin, Alaska, U.S.A., *Arct. Alp. Res.*, *29*(4), 367–378.
Nelson, F. E., K. M. Hinkel, N. I. Shiklomanov, G. R. Mueller, L. L. Miller, and D. A. Walker (1998), Active-layer thickness in north central Alaska: Systematic sampling, scale, and spatial autocorrelation, *J. Geophys. Res.*, *103*(D22), 28,963–28,973, doi:10.1029/98JD00534.
Nelson, F. E., N. I. Shiklomanov, and G. R. Mueller (1999), Variability of active-layer thickness at multiple spatial scales, North-Central Alaska, U.S.A., *Arct. Antarct. Alp. Res.*, *31*(2), 179–186.
Nixon, F. M., A. E. Taylor, V. S. Allen, and F. Wright (1995), Active layer monitoring in natural environments, lower Mackenzie Valley, Northwest Territories, in *Current Research, 1995-B*, 99–108, Geol. Surv. of Can., Ottawa, Canada.
Park, C. N., and A. L. Dudycha (1974), A cross-validation approach to sample size determination for regression models, *J. Am. Stat. Assoc.*, *69*(345), 214–218, doi:10.1080/01621459.1974.10480156.
Pavlov, A. V. (1975), *Heat Transfer of the Soil and Atmosphere at Northern and Temperate Latitudes of the USSR*, Yatkutsk, 302 pp, Joint Publications Research Service, Arlington, Va. [USA/CRREL Draft Transl. 551].
Porter, D. F., J. J. Cassano, and M. C. Serreze (2011), Analysis of the Arctic atmospheric energy budget in WRF: A comparison with reanalyzes and satellite observations, *J. Geophys. Res.*, *116*, D22108, doi:10.1029/2011JD016622.
Rickard, W., and J. Brown (1972), The performance of a frost tube for the determination of soil freezing and thawing depths, *Soil Sci.*, *113*, 149–154, doi:10.1097/00010694-197202000-00011.
Romanovsky, V. E., and T. E. Osterkamp (1995), Interannual variations of the thermal regime of the active layer and near-surface permafrost in northern Alaska, *Permafrost Periglacial Processes*, *6*, 313–335, doi:10.1002/ppp.3430060404.
Romanovsky, V. E., M. Burgess, S. Smith, K. Yoshikawa, and J. Brown (2002), Permafrost temperature records: Indicators of climate change, *Eos Trans. AGU*, *83*(50), 589–594, doi:10.1029/2002EO000402.

Rosswall, T., and O. W. Heal (Eds.) (1975), Structure and function of Tundra ecosystems: Papers Presented at the IBP Tundra Biome V International Meeting on Biological Productivity of Tundra, Abisko, Sweden, April 1974, *Ecol. Bull. 20*, 450 pp., Swedish Nat. Sci. Res. Counc., Stockholm.

Rowland, J. C., et al. (2010), Arctic landscapes in transition: responses to thawing permafrost, *Eos Trans. AGU*, *91*(26), 229–230, doi:10.1029/2010EO260001.

Shiklomanov, N. I., and F. E. Nelson (1999), Analytic representation of the active layer thickness field, Kuparuk River Basin, Alaska, *Ecol. Modell.*, *123*(2–3), 105–125, doi:10.1016/S0304-3800(99)00127-1.

Shiklomanov, N. I., D. A. Streletskiy, F. E. Nelson, R. D. Hollister, V. E. Romanovsky, C. E. Tweedie, J. G. Bockheim, and J. Brown (2010), Decadal variations of active-layer thickness in moisture-controlled landscapes, Barrow, Alaska, *J. Geophys. Res.*, *115*, G00I04, doi:10.1029/2009JG001248.

Shrestha, R. L., W. E. Carter, M. Lee, P. Finer, and M. Sartori (1999), Airborne laser swath mapping: Accuracy assessment for surveying and mapping applications, *J. Am. Congr. Surv. Mapp.*, *59*(2), 83–94.

Slater, A. G., and D. M. Lawrence (2013), Diagnosing present and future permafrost from climate models, *J. Clim.*, *26*(15), 5608–5623, doi:10.1175/JCLI-D-12-00341.1.

Smith, M. W. (1975), Microclimate influences on ground temperatures and permafrost distribution, Mackenzie Delta, Northwest Territories, *Can. J. Earth Sci.*, *12*(8), 1421–1438, doi:10.1139/e75-129.

Smith, M. W., and D. W. Riseborough (2002), Climate and the limits of permafrost: A zonal analysis, *Permafrost Periglacial Processes*, *13*(1), 1–15, doi:10.1002/ppp.410.

Smith, S. L., S. A. Wolfe, D. W. Riseborough, and F. M. Nixon (2009), Active-layer characteristics and summer climatic indices, Mackenzie valley, Northwest Territories, Canada, *Permafrost Periglacial Processes*, *20*(2), 201–220, doi:10.1002/ppp.651.

Stevens, J. (2002), *Applied Multivariate Statistics for the Social Sciences*, 4th ed., Lawrence Erlbaum Assoc., Mahwah, N. J.

Streletskiy, D. A., N. I. Shiklomanov, and F. E. Nelson (2012), Spatial variability of permafrost active-layer thickness under contemporary and projected climate in northern Alaska, *Polar Geogr.*, *35*(2), 95–116, doi:10.1080/1088937X.2012.680204.

Tarnocai, C., J. G. Canadell, E. A. G. Schuur, P. Kuhry, G. Mazhitova, and S. Zimov (2009), Soil organic carbon pools in the northern circumpolar permafrost region, *Global Biogeochem. Cycles*, *23*, GB2023, doi:10.1029/2008GB003327.

Taylor, A. E. (2000), Relationship of ground temperatures to air temperatures in forests, in *The Physical Environment of the Mackenzie Valley, Northwest Territories: A Base Line for the Assessment of Environmental Change, Geol. Sur. Can. Bull*. 547, edited by L. D. Dyke and C. R. Brooks, pp. 111–117, Natural Resources Canada, Ottawa, Canada.

Thompson, S. K. (2012), *Sampling*, 3rd ed., 436 pp., John Wiley, N. Y.

Updike, T., and C. Comp (2010), Radiometric use of WorldView-2 imagery, *Technical Note, Revision 1.0*, DigitalGlobe, Longmont, Colo.

Villarreal, S., R. D. Hollister, D. R. Johnson, M. J. Lara, P. J. Webber, and C. E. Tweedie (2012), Tundra vegetation change near Barrow, Alaska (1972–2010), *Environ. Res. Lett.*, *7*(1), 015508, doi:10.1088/1748-9326/7/1/015508.

Webber, P. J. (1978), Spatial and temporal variation of the vegetation and its productivity, in *Vegetation and Production Ecology of an Alaskan Arctic Tundra*, pp. 37–112, Springer, N. Y., doi:10.1007/978-1-4612-6307-4-3.

Williams, P. J., and M. W. Smith (1989), *The Frozen Earth, Fundamentals of Geocryology Studies in Polar Research Series*, 306 pp., Cambridge Univ. Press, Cambridge, U. K.

Willmott, C. J. (1981), On the validation of models, *Phys. Geogr.*, *2*, 184–194, doi:10.1080/02723646.1981.10642213.

Willmott, C. J. (1982), Some comments on the evaluation of model performance, *Bull. Am. Meteorol. Soc.*, *63*, 1309–1313, doi:10.1175/1520-0477(1982)063 <1309:SCOTEO> 2.0.CO;2.

Willmott, C. J., and K. Matsuura (2005), Advantages of the mean absolute error (MAE) over the root mean square error (RMSE) in assessing average model performance, *Clim. Res.*, *30*, 79–82, doi:10.3354/cr030079.

Zhang, T., T. E. Osterkamp, and K. Stamnes (1997), Effects of climate on the active layer and permafrost on the north slope of Alaska, U.S.A., *Permafrost Periglacial Processes*, *8*(1), 45–67, doi:10.1002/(SICI)1099-1530(199701)8:1<45::AID-PPP240>3.0.CO;2-K.

Zhang, T., et al. (2005), Spatial and temporal variability in active layer thickness over the Russian Arctic drainage basin, *J. Geophys. Res.*, *110*, D16101, doi:10.1029/2004JD005642.

Zona, D., D. A. Lipson, S. F. Zulueta, R. C. Oberbauer, and W. C. Oechel (2011), Microtopographic controls on ecosystem functioning in the arctic coastal plain, *J. Geophys. Res.*, *116*, G00I08, doi:10.1029/2009JG001241.